



GALACTIC COSMIC RAY RADIATION LEVELS IN SPACECRAFT ON INTERPLANETARY MISSIONS

J. L. Shinn,* J. E. Nealy,* L. W. Townsend,* J. W. Wilson* and
J. S. Wood**

* *National Aeronautics and Space Administration, Langley Research Center,
Hampton, VA 23681, U.S.A.*

** *Flight Mechanics and Control, Inc., Hampton, VA 23669, U.S.A.*

ABSTRACT

Using the Langley Research Center galactic cosmic ray (GCR) transport computer code (HZETRN) and the computerized anatomical man (CAM) model, crew radiation levels inside manned spacecraft on interplanetary missions are estimated. These radiation-level estimates include particle fluxes, LET (linear energy transfer) spectra, absorbed dose, and dose equivalent within various organs of interest in GCR protection studies. Changes in these radiation levels resulting from the use of various different types of shield materials are presented.

INTRODUCTION

Manned interplanetary space travel will involve long periods away from the protective cover of the Earth's magnetosphere to the regions where there exists the possibility of serious biological injury from galactic cosmic rays (GCR) and energetic solar particle events (SPE). For an SPE, the major concerns are acute effects arising from sudden exposure to very large radiation doses of solar protons. The severeness of these effects can be reduced when protective shieldings such as storm shelters are adequately provided /1, 2/. On the other hand, the cumulative exposure to the low level, high-LET (linear energy transfer) components of GCR poses a challenge to the radiation protection community. Not only is there a lack of human data to assess the effects of high-LET particles, but also for lack of nuclear fragmentation data, large uncertainties exist in the predictions of projectile fragments as heavy GCR components break up along their paths inside the target medium /3/. For the present, the risk assessments and related shield requirements are made using the quality factor established for more conventional low-LET radiations. Various sensitive organ doses are estimated using a realistic human body geometry whereby the effect of self-shielding is accounted for /4/. In reference 5, preliminary estimates of dose equivalent for skin, ocular lens, and bone marrow were computed assuming the astronaut represented by the CAM model to be at the center of a large, spherical, aluminum spacecraft of uniform thickness for missions beyond Earth's magnetosphere during the solar minimum period of the solar cycle. The calculations were made using a computer-efficient, deterministic galactic cosmic ray transport code, HZETRN /6/, developed at Langley Research Center. The quality factor of ICRP 26 /7/ was assumed. In this paper, we extend the work of reference /5/ to estimate particle fluxes, and differential and integral LET-spectra, in addition to the usually estimated absorbed doses and dose equivalents. The sensitive organs considered are the ocular lens, thyroid gland, and bone marrow. The new

quality factor of ICRP 60 /8/ is assumed. Effects of using representative shielding materials of different nuclear properties on the radiation levels are also studied.

GCR TRANSPORT THEORY

In transversing extended matter, heavy ions lose energy through interaction with atomic electrons along their trajectories. On occasion, they interact violently with nuclei of the matter, producing ion fragments moving in the forward direction and low energy fragments of the struck target nucleus. The transport equations for the short range target fragments can be solved in closed form in terms of collision density /9/. This leads to the projectile fragment transport as the remaining problem of interest. In previous work /10/, the projectile ion fragments were treated as if all went straight ahead because of the large kinetic energy possessed by the projectile, and the fragmentation mechanism. The straight-ahead approximation is found to be quite accurate for the nearly isotropic cosmic ray fluence /9/.

Using the straight-ahead approximation, the transport equation is written in one-dimensional form

$$\left[\frac{\partial}{\partial x} - \frac{\partial}{\partial E} S_j(E) + \sigma_j \right] \Phi_j(x, E) = \sum_{k>j} m_{jk} \sigma_k \Phi_k(x, E) \quad (1)$$

where $\Phi_j(x, E)$ is the flux of ions of type j with atomic mass A_j at x moving along the x -axis at energy E in units of MeV/amu, σ_j is the corresponding macroscopic nuclear absorption cross section, $S_j(E)$ is the change in E per unit distance, and m_{jk} is the multiplicity of ion j produced in collision by ion k . The corresponding nucleon transport equation /11-13/ is

$$\left[\frac{\partial}{\partial x} - \frac{\partial}{\partial E} S_j(E) + \sigma_j(E) \right] \Phi_j(x, E) = \sum_k \int_E^\infty \sigma_{jk}(E, E') \Phi_k(x, E') dE' \quad (2)$$

The m_{jk} , and σ_j are assumed energy independent in equation (1) for the current version of HZETRN, and the full energy dependence is retained in equation (2). Using characteristic variables, equations (1) and (2) can be transformed to simpler differential equations which are easily integrated. Further use of a perturbation expansion in the solution /14/ results in, for heavy ions

$$\Psi_j(x+h, r_j) = e^{-\sigma_j h} \Psi_j(x, r_j+h) + \sum_k m_{jk} \sigma_k \frac{\nu_j}{\nu_k} \left(\frac{e^{-\sigma_j h} - e^{-\sigma_k h}}{\sigma_k - \sigma_j} \right) \Psi_k \left(x, r_k + \frac{\nu_j}{\nu_k} h \right) \quad (3)$$

where $\nu_j = Z_j^2/A_j$, $\Psi_j = S_j \Phi_j$ and $r_j = r/\nu_j$ with r being the proton range which is related to energy E . Equation (3) is readily seen as a stepping formalism which will propagate the solution from the surface boundary into the shield thickness in a step size of h . The corresponding propagating formalism for the nucleons is given as /12/

$$\Psi(x+h, r) \approx e^{-\sigma h} \Psi(x, r+h) + e^{-\sigma h} \int_0^h dz \int_r^\infty dr' \bar{f}(r+z, r'+z) \Psi(x, r'+h) \quad (4)$$

where $\bar{f} = S \sigma_{jk}$. The numerical procedures for evaluating the integral in equation (4) for the production of secondary nucleons and other numerical issues are discussed elsewhere /11,12/. Once Ψ is determined from equations (3) and (4), the fluxes for each ion Φ_j is then easily obtained by reverse transformation.

GCR DOSE ASSESSMENT

After the particle fluxes for each GCR ion have been determined, the absorbed dose is computed from

$$D_i(x, >E) = A_i \int_E^\infty S_i(E') \cdot \Phi_i(x, E') dE' \quad (5)$$

The dose equivalent is obtained from

$$H_i(x, >E) = A_i \int_E^{\infty} Q_i [S(E')] \cdot S(E') \cdot \Phi_i(x, E') dE' \quad (6)$$

where Q denotes the quality factor which relates absorbed dose to the risk. In this paper, the LET-dependent values from ICRP-60 are used. Here, the stopping power, S and linear energy transfer, L are numerically equal. The dose and dose equivalent as given by equations (5) and (6) include contributions from projectiles and projectile fragments for the heavy ions. Target fragment contributions can be evaluated separately with flux given in a closed form. This has been discussed elsewhere /7,9/ and will not be repeated.

For the organ exposure estimates in this work, the incident GCR spectra (solar minimum periods) obtained from the Naval Research Laboratory CREME model /15/ are transported through the appropriate thickness of shield and then through an additional 100 g/cm² of water. The fluence at solar minimum of the incident ions $Z = 1$ to 28 based on the CREME model are displayed in Figure 1, indicating the abundance of even-charge ions over the odd. The computed dose/dose equivalent as a function of water depth then becomes the input to a standing human geometry model. In the Computerized Anatomical Man (CAM) model /16/, the depth distribution at a particular organ site is approximated using a 512-ray distribution over a 4π solid angle. The dose/dose equivalent at each organ site is then obtained by folding the dose/dose equivalent versus water depth into the organ-depth distribution /4/. For the blood forming organ (BFO) considered in this study, an average distribution of 33 different sites are used. Figure 2, displays the depth distributions for ocular lens, thyroid, and average BFO representing a rather shallow organ, moderately shielded organ, and a deeply shielded organ, respectively.

RESULTS AND DISCUSSION

The quality factor which relates absorbed dose to dose equivalent (closely related to radiation risk) is usually taken to be the maximum RBE (relative biological effectiveness) obtained when the dose approaches zero /17/. There is evidence suggesting that RBE depends on many other factors besides LET /18/; however, the distribution of exposure components over LET is still a primary indicator of biological response for GCR exposure. For example, low-LET components allow certain biological repairs at low dose rates and correspond to a lower risk. High-LET components can show enhanced biological effects at low dose rates and generally high RBE values. Thus, the possibility of altering various LET components through the choice of materials becomes an important aspect of spacecraft shield design for manned space missions. In the following, we first examine how the choice of shield material and its thickness changes the internal environment within the spacecraft, and then discuss the effects of body self-shielding on organ exposures. Estimates of radiation

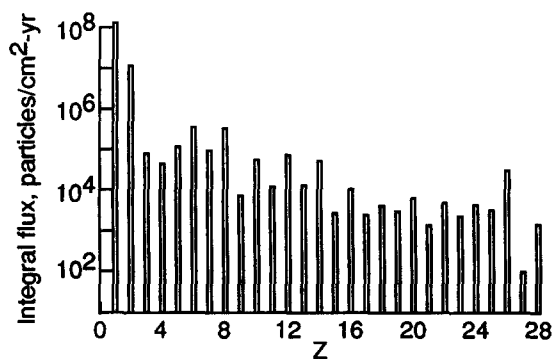


Fig. 1. Annual GCR integral flux in free space as function of ion charge at solar minimum.

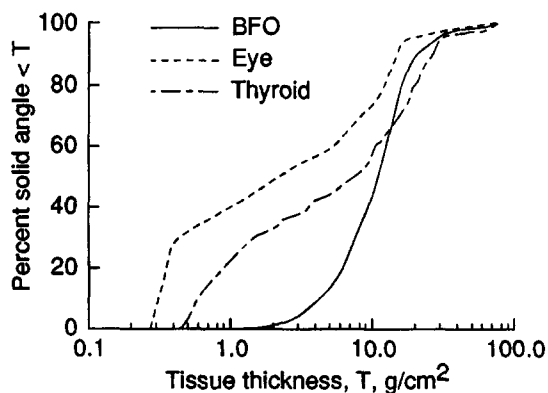


Fig. 2. Body-organ-depth distributions for the ocular lens, thyroid, and bone marrow (BFO) according to the CAM model.

levels inside the spacecraft and body organs for the solar minimum GCR environment have been determined utilizing the methods outlined in the previous sections. Note that the use of an old version of HZETRN here introduces small variations in doses among some published results but does not alter the qualitative results which we are currently interested in.

Internal Environment

The high-LET radiation components are usually degraded to lower-LET as a result of nuclear interactions between projectile and target nuclei and such processes become more significant as the particles penetrate further into the shield medium. This is illustrated in Figure 3 where integral fluxes of all the ions are plotted as a function of LET at several depths (2, 5, and 10 g/cm²) of aluminum. Similar trends as shown in Figure 3 will hold for other shield materials such as polyethylene and iron. However, when the latter two are compared to aluminum for flux distribution over LET at these three different depths (see Figures 4–6), polyethylene is the most effective high-LET degrader beyond 5 g/cm² but actually is the least at 2 g/cm². The differences between iron and aluminum are in general not as significant. Comparisons of each individual ion flux for iron and polyethylene shields with respect to aluminum are shown in Figures 7–9 for these different depths. Again, they show little variations for all the ions between aluminum and iron. The large overshoots for polyethylene are seen to occur for odd-charge ions which are less abundant compared to the even-charge ions.

The dependence of the internal environment on the shield composition results from the differences in atomic cross sections, nuclear attenuation, and the distribution of fragmentation products. The large nuclear attenuation for the polyethylene shield can in part be seen from the relatively large loss of Fe ($Z = 26$) and Ni ($Z = 28$) in polyethylene compared to iron or aluminum shielding. These fragmentations in polyethylene contribute substantially to the Co ($Z = 27$) and Mn ($Z = 25$) flux relative to both iron and aluminum shields. Since the ΔZ in fragmentation /19/ by polyethylene is smaller than that by iron or aluminum, the thin polyethylene seems to enhance the high-LET flux in comparison. Also, because of the higher nuclear attenuation rate in polyethylene than in either aluminum or iron shields, the second fragmentation event occurs more often in the thicker polyethylene shields for which the second ΔZ shift greatly reduces the high-LET components in polyethylene. This is most apparent in the prominent peaks in the thicker polyethylene targets for

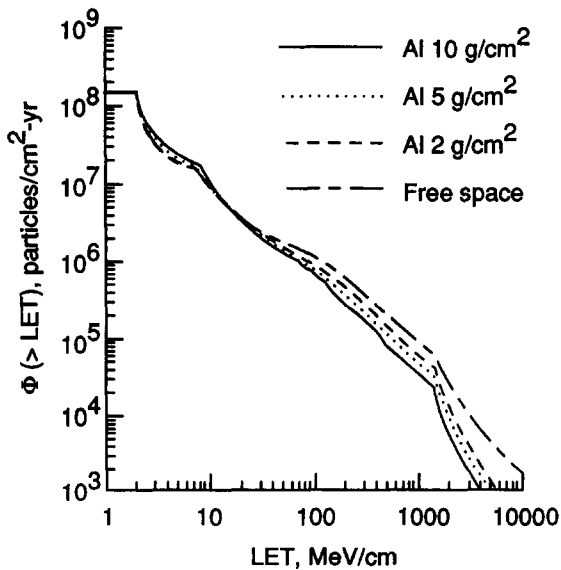


Fig. 3. LET-spectra for annual GCR integral flux in free space and behind various thicknesses of aluminum shield at solar minimum.

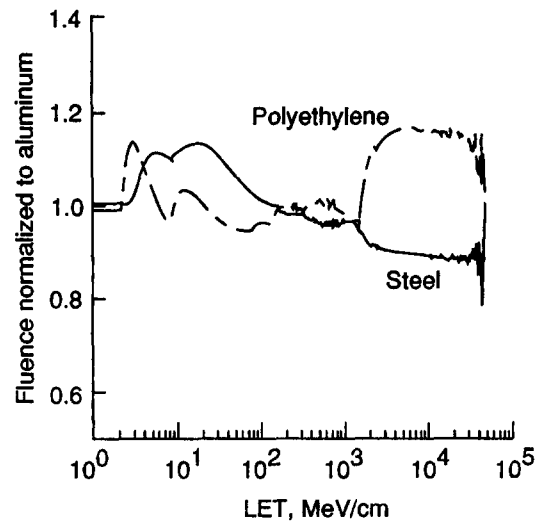


Fig. 4. Comparison of LET-spectra for flux in transmitted GCR through polyethylene or iron shield with respect to aluminum for 2 g/cm² in shield thicknesses at solar minimum.

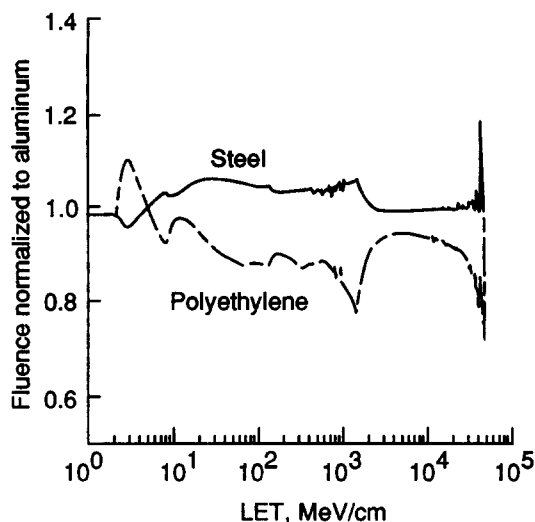


Fig. 5. Comparison of LET-spectra for flux in transmitted GCR through polyethylene or iron shield with respect to aluminum for 5 g/cm² in shield thicknesses at solar minimum.

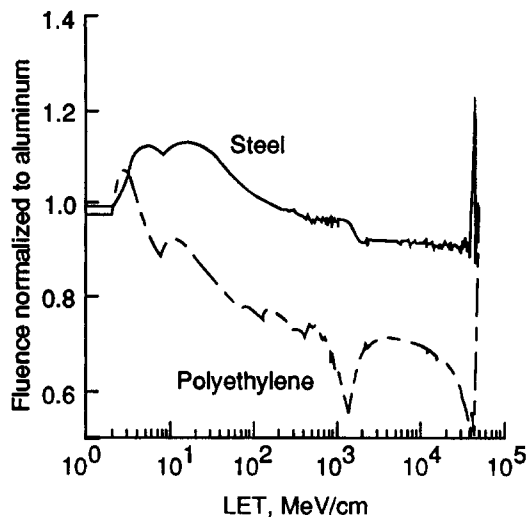


Fig. 6. Comparison of LET-spectra for flux in transmitted GCR through polyethylene or iron shield with respect to aluminum for 10 g/cm² in shield thicknesses at solar minimum.

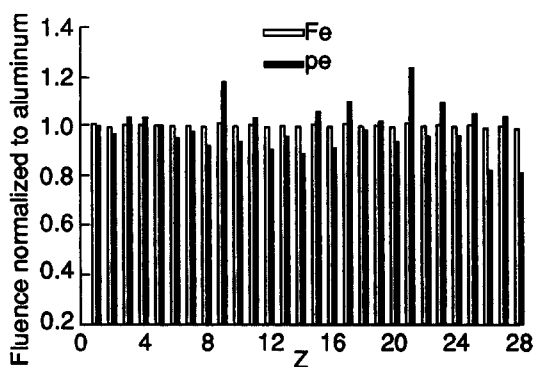


Fig. 7. Comparison of ion abundance in transmitted GCR through polyethylene or iron shield with respect to aluminum for 2 g/cm² in shield thicknesses at solar minimum.

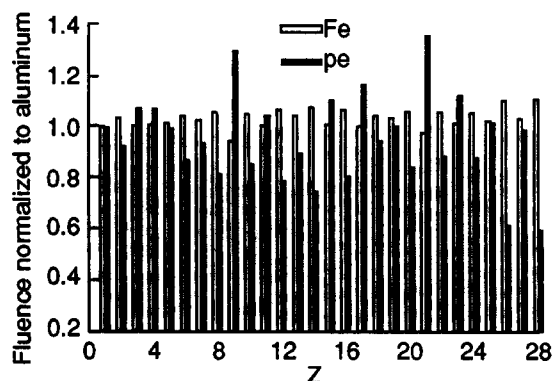


Fig. 8. Comparison of ion abundance in transmitted GCR through polyethylene or iron shield with respect to aluminum for 5 g/cm² in shield thicknesses at solar minimum.

$Z = 21, 17, 15,$ and 9 (Figures 8–9). Although a final assessment of which LET distribution is most either aluminum or iron shields, the second fragmentation event occurs more often in the thicker polyethylene shields for which the second ΔZ shift greatly reduces the high-LET components in polyethylene. This is most apparent in the prominent peaks in the thicker polyethylene targets for $Z = 21, 17, 15,$ and 9 (Figures 8–9). Although a final assessment of which LET distribution is most advantageous must await clarification of the biological response function, it has been demonstrated that reasonable control over the LET distribution can be achieved by a suitable choice of shield material at fixed shield mass. The optimum design must await further biological study.

Radiation Levels in Body Organs

Depending on how deeply organs are embedded inside the body, the surrounding tissue (which is assumed to be 100-percent water) can be considered to be a reasonably good shield because of

the similar nuclear properties which water and polyethylene possess. For the three organ depth-distributions shown in Figure 2, ocular lens is the least shielded, BFO the most, and thyroid slightly better than ocular lens. Assuming the astronaut is at the center of a spherical, spacecraft of 5 g/cm^2 thickness, the radiation levels for these three organs are estimated using aluminum, polyethylene, and iron separately as the shield. The results for the total dose equivalents are listed in Table 1. It is clear, from the table, that the equivalent sphere approximation is conservative when used to represent the actual BFO exposure. It is also seen that for the same organ, polyethylene is the best shield and iron slightly worse than aluminum. When the integral LET-spectra using polyethylene or iron shield are compared relative to aluminum shield for the dose (Figure 10) and dose equivalent (Figure 11) received at BFO and ocular lens, a reduction of about 25–30 percent in high LET components for polyethylene is noted. Figures 12–14 display the changing contribution indose equivalent for each individual ion beginning from the external environment, to ocular lens and BFO with 5 g/cm^2 aluminum shield. The dose equivalent from the iron ions was highest among all the ions in the free space but became only slightly lower than that of protons for the ocular lens and diminishingly less important for the BFO where all the heavy ions are seen to be equalized by the large amount of (water) tissue. The uncertainty which currently exists in relating absorbed dose to dose equivalent for high-LET particles is a major concern in the risk estimates for manned

TABLE 1 Annual Solar Minimum Galactic Cosmic-Ray Dose Equivalent*, ** (cSv) for Various Organs within Spacecraft of 5 g/cm^2 of Various Shield Material

Shield Material	Ocular Lens	Thyroid Gland	Bone Marrow	5-cm Equivalent Sphere
Aluminum	57.8	50.1	43.3	54.2
Polyethylene	47.3	41.8	36.9	45.0
Iron	62.9	54.1	45.8	58.1

* Quality factor recommended in ICRP-60 is assumed.

** All the values shown above do not include target fragments contributions which were estimated to be approximately 5 cSv.

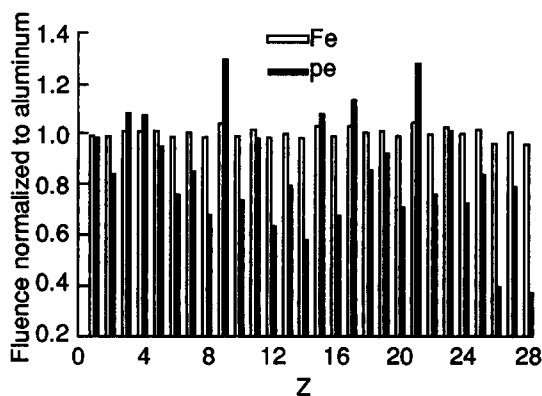


Fig. 9. Comparison of ion abundance in transmitted GCR through polyethylene or iron shield with respect to aluminum for 10 g/cm^2 in shield thicknesses at solar minimum.

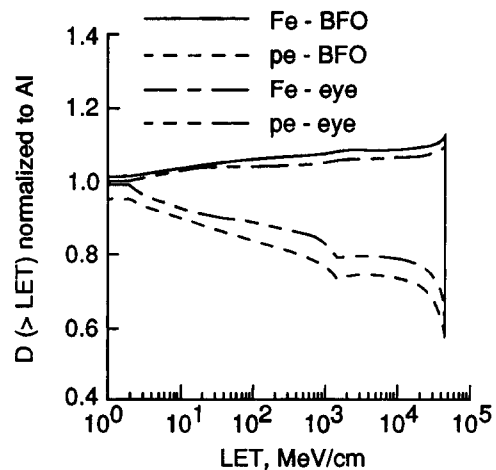


Fig. 10. Normalized integral LET-spectra for GCR absorbed dose at BFO and ocular lens for the astronaut at the center of a spherical spacecraft of uniform thickness at solar minimum. The spectra for polyethylene or iron shields are normalized to aluminum. The shields are 5 g/cm^2 in thickness.

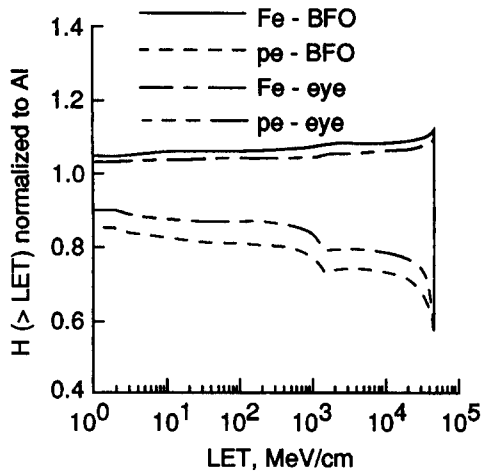


Fig. 11. Normalized integral LET-spectra for GCR dose equivalent at BFO and ocular lens for the astronaut at the center of a spherical spacecraft of uniform thickness at solar minimum. The spectra for polyethylene or iron shields are normalized to aluminum. The shields are 5 g/cm^2 in thickness.

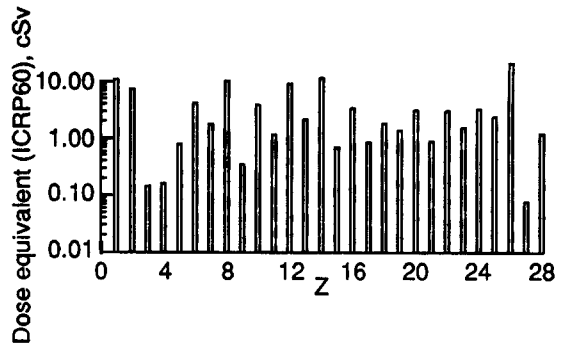


Fig. 12. Annual dose equivalent in free space as a function of ion charge for GCR at solar minimum.

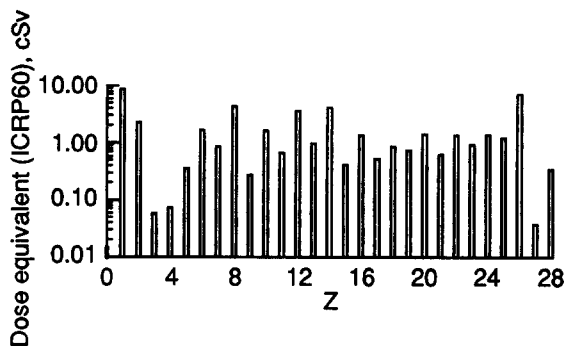


Fig. 13. Annual dose equivalent at ocular lens as a function of ion charge from GCR exposure at solar minimum. The astronaut is at the center of a spherical, aluminum spacecraft of uniform thickness of 5 g/cm^2 .

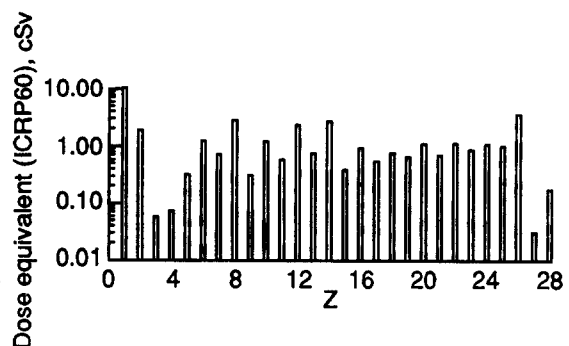


Fig. 14. Annual dose equivalent at BFO as a function of ion charge from GCR exposure at solar minimum. The astronaut is at the center of a spherical, aluminum spacecraft of uniform thickness of 5 g/cm^2 .

space missions. Considering the case of an aluminum spacecraft of 5 g/cm^2 thickness, the differential LET-spectra corresponding to the dose and dose equivalent which the astronaut receives (excluding the small contribution from neutron and target fragments) in one year, for the BFO and ocular lens, are shown in Figures 15–16, respectively. The spikes seen in the figures correspond to the zero slope of stopping power ($dL/dE = 0$) at minimum ionization (2 GeV/nucleon) of each ion $/Z/$ with protons starting at the lowest LET followed by increasing Z for the increasing L . The sharp peak at the highest LET is the Bragg peak when the ions nearly come to rest. Since the LET coordinate is scaled in logarithm, the differential dose LdN/dL is converted to $L^2 dN/dL$, where $N = \int \Phi dE$ so that the area under the curve is linearly proportional to the total dose. Similarly, the differential dose equivalent is plotted as $QL^2 dN/dL$. For the high-LET region ($L > 100 \text{ MeV/cm}$), the area bounded by the differential dose curve is a comparatively small contribution to the total dose, yet the area under the differential dose equivalent contributes more than the low-LET region. The magnification in dose equivalent at the high-LET regions is a reflection of the ICRP-60 quality

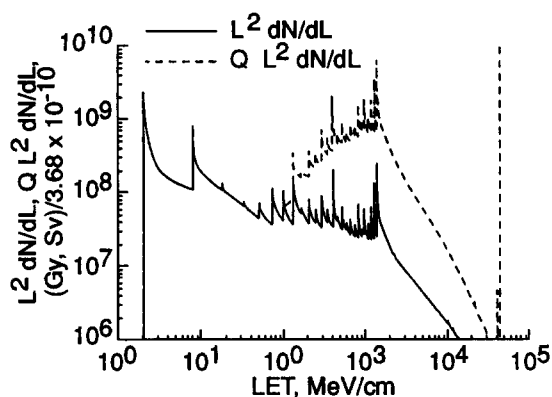


Fig. 15. Differential LET-spectra for annual dose and dose equivalent at BFO from GCR exposure at solar minimum. The astronaut is at the center of a spherical, aluminum spacecraft of uniform thickness of 5 g/cm².

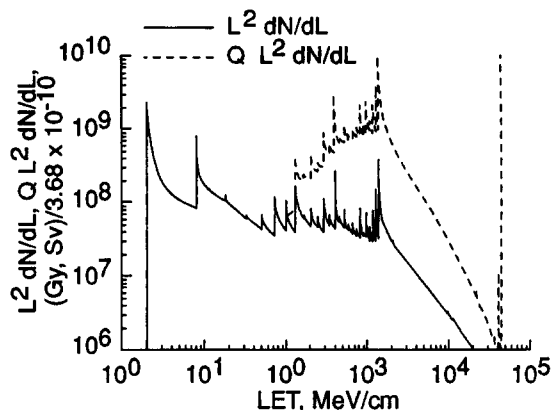


Fig. 16. Differential LET-spectra for annual dose and dose equivalent at ocular lens from GCR exposure at solar minimum. The astronaut is at the center of a spherical, aluminum spacecraft of uniform thickness of 5 g/cm².

factor. Depending on the outcome of future biological response model for heavy ions, the large contribution from high-LET region may vary the total dose equivalent significantly.

CONCLUDING REMARKS

Estimates of crew radiation levels inside manned spacecraft on interplanetary missions during solar minimum period were made in terms of particle flux, integral/differential LET-spectra, and dose/dose equivalent using the Langley Research Center galactic transport code (HZETRN). It was demonstrated that reasonable control over the LET distribution for the radiation inside the spacecraft can be achieved by choice of shield material at fixed shield mass. Assuming the nuclear fragmentation physics contained in HZETRN is fairly correct, it seems that the lighter materials such as polyethylene and water enhance the high-LET components relative to aluminum for thin shields and reduce the high-LET components more efficiently than aluminum or iron for thick shields. For the same reason, the deeply shielded bone marrow is best protected by the surrounding tissue (water) compared to the thyroid and ocular lens, of which the thyroid is slightly better shielded. Comparing the differential LET-spectra for dose and dose equivalent at the organ sites, it was shown that the uncertainties which exist in relating absorbed dose to dose equivalent will affect the risk estimates very significantly. Future efforts to reduce the uncertainties in biological response models for heavy ions as well as nuclear fragmentation models must be made.

REFERENCES

1. L.W. Townsend, J.L. Shinn, and J.W. Wilson, Interplanetary crew exposure estimates for the August 1972 and October 1989 solar particle events. *Radiat. Res.*, #126, 108-110 (1991).
2. L.W. Townsend, J.W. Wilson, J.L. Shinn, and S.B. Curtis, Human exposure to large solar particle events in space. *Adv. Space Res.* #12, 339-348 (1992).
3. J.W. Wilson, L.W. Townsend, W. Schimmerling, G.S. Khandelwal, F. Khan, J.E. Nealy, F.A. Cucinotta, L.C. Simonsen, J.L. Shinn, and J.W. Norbury, Transport methods and interactions for space radiations. *NASA RP 1257* (December 1991).
4. J.L. Shinn, J.W. Wilson, and J.E. Nealy, Reliability of equivalent sphere model in blood-forming organ dose estimation. *NASA TM 4178* (April 1990).

5. L.W. Townsend, F.A. Cucinotta, and J.W. Wilson, Interplanetary crew exposure estimates for galactic cosmic rays. *Radiat. Res.*, #129, 48-52 (1992).
6. J.W. Wilson, S.Y. Chun, F.F. Badavi, L.W. Townsend, and S.L. Lamkin, HZETRN: A heavy ion/nucleon transport code for space radiations. *NASA TP 3146* (December 1991).
7. ICRP, Recommendations of the ICRP, Publication 26, Annals of the ICRP, No. 3 Pergamon, New York, (1977).
8. ICRP, Recommendations of the International Commission on Radiological Protection, Publication 60, Annals of the ICRP, Vol. 21, No. 1-3. Pergamon, New York, (1991).
9. J.W. Wilson, Analysis of the theory of high-energy ion transport. *NASA TN D-8381* (March 1977).
10. J.W. Wilson, Heavy ion transport in the straight ahead approximation. *NASA TP-2178* (June 1983).
11. J.L. Shinn, J.W. Wilson, M. Weyland, and F.A. Cucinotta, Improvements in computational accuracy of BRYNTRN (A Baryon Transport Code). *NASA TP-3093* (May 1991).
12. J.W. Wilson, L.W. Townsend, J.E. Nealy, S.Y. Chun, B.S. Hong, W. Buck, S.L. Lamkin, B.D. Ganapol, F. Khan, and F.A. Cucinotta: BRYNTRN: A Baryon Transport Model. *NASA TP-2887* (March 1989).
13. J.L. Shinn, J.W. Wilson, J.E. Nealy, and F.A. Cucinotta: Comparison of dose estimates using the buildup-factor method and a baryon transport code (BRYNTRN) with monte carlo results. *NASA TP-3021* (October 1990).
14. J.W. Wilson and S.L. Lamkin: Perturbation theory for charged-particle transport in one dimension. *Nucl. Sci. & Eng.* #57 (August 1975).
15. J.H. Adams, Cosmic ray effects on microelectronics, part IV. Naval Research Laboratory Memorandum Report 5901 (revised), Washington, DC (1987).
16. R.W. Langley and M.P. Billings, A new model for estimating space proton dose to body organs. *Nucl. Technol.*, #15, 68-74 (1972).
17. W.K. Sinclair: Experimental RBE values of high LET radiations at low doses and the implications for quality factor assignment. *Radiat. Prot. Dosim.*, #13, 319-326 (1985).
18. H.J. Schaefer: Exposure hazards from cosmic radiation beyond the stratosphere and in free space. *J. Aviation Med.*, #23, 334-344 (1952).
19. J.W. Wilson, L.W. Townsend, and F.F. Badavi, Galactic HZE propagation through the Earth's atmosphere, *Radiat. Res.*, #109, 173-183 (1987).
20. J.W. Wilson and F.F. Badavi, A study of the generation of LET spectra for space radiations, *NASA TP* (In press).